

# Laser cooling a centimeter-scale torsion pendulum

Dong-Chel Shin,<sup>1,\*</sup> Tina Hayward,<sup>2</sup> Dylan Fife,<sup>1</sup> Rajesh Menon,<sup>2</sup> and Vivishek Sudhir<sup>1,3,†</sup>

<sup>1</sup>*Department of Mechanical Engineering, Massachusetts Institute of Technology, Cambridge, MA 02139*

<sup>2</sup>*Department of Electrical and Computer Engineering, University of Utah, Salt Lake City, Utah 84112*

<sup>3</sup>*LIGO Laboratory, Massachusetts Institute of Technology, Cambridge, MA 02139*

(Dated: September 5, 2024)

Torsion pendula have long been pivotal in the study of classical gravitational forces. Experimental tests of gravity’s fundamental nature call for mechanical systems in the quantum regime while being sensitive to gravity. We laser cool a centimeter-scale torsion pendulum to a temperature of 10 mK (average occupancy of 6000 phonons) starting from room temperature (equivalent to  $2 \cdot 10^8$  phonons). This is achieved by optical radiation pressure forces conditioned on a quantum-noise-limited optical measurement of the pendulum’s angular displacement with an imprecision 13 dB below that at the standard quantum limit (SQL). The measurement sensitivity is the result of a novel ‘mirrored’ optical lever that passively rejects extraneous spatial-mode noise by 60 dB. The high mechanical quality ( $10^7$ ) and quantum-noise-limited sub-SQL measurement imprecision demonstrate the necessary ingredients for realizing the quantum ground state of torsional motion — a pre-requisite for mechanical tests of gravity’s alleged quantum nature.

*Introduction.* Torsion pendula have long been pivotal in the measurement of weak fundamental forces, most notably in establishing the electrostatic inverse-square law [1, 2], precision measurements of classical gravitational forces [3–7], tests of the equivalence principle [8–11], and the first observation of radiation pressure torque [12]. In all these experiments, the torsion pendulum is employed as a sensor for a weak classical force.

Recent interest in observing gravity’s alleged quantum nature calls for experiments where gravitationally attracting macroscopic mechanical oscillators are simultaneously prepared in quantum states of their motion [13–15]. Torsion pendula are particularly suited for such experiments on account of the low thermal Brownian noise of torsional suspensions even when mass-loaded [16, 17], and well-understood techniques for isolating gravitational interaction between them even with masses as small as 100 mg [18]. However, in contrast to the mature array of techniques available for quantum-limited measurement and control of linear motion within the field of cavity optomechanics [19], experimental realization of similar techniques has remained elusive for torsional motion.

In this letter we demonstrate laser cooling of a centimeter-scale high-quality torsion pendulum using a novel “mirrored optical lever” whose quantum-noise-limited sensitivity of  $10^{-12}$  rad/ $\sqrt{\text{Hz}}$  is 13 dB below the zero-point motion of the pendulum. Conditioned on this measurement, we apply optical radiation pressure torque on the pendulum so as to cool its angular motion to 10 mK from room temperature, corresponding to an average phonon occupation of  $5964 \pm 39$  (starting from  $\sim 2 \times 10^8$ ). In the following, we describe the torsion pendulum, the mirrored optical lever used to measure its angular motion, its performance in terms of classical noise cancellation, its

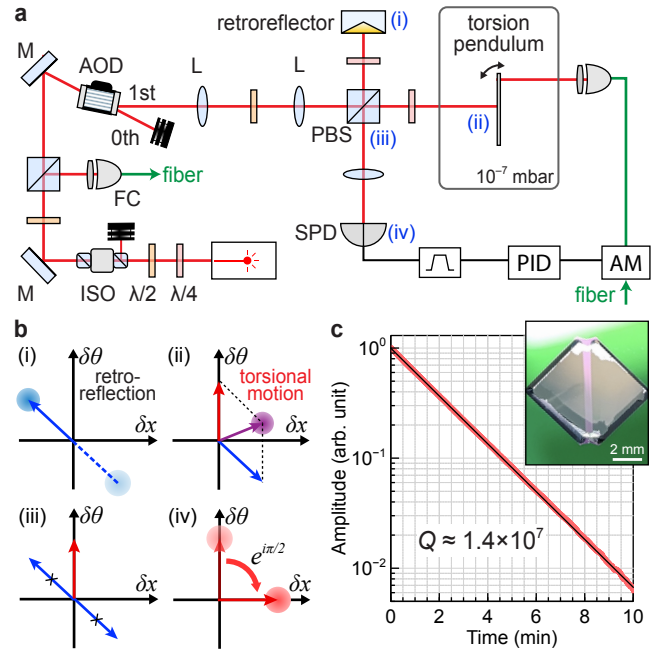


FIG. 1. (a) Experimental setup: 1064 nm light in the fundamental spatial mode is used to measure and actuate a cm-scale torsion pendulum (panel (c)). The acousto-optic deflector (AOD) and the  $4f$  lens system is used to calibrate the mirrored optical lever that follows it. (b) Principle of classical noise suppression in the mirrored optical lever (see text for details) (c) A cm-scale torsion pendulum fabricated in tensile-stressed SiN (inset) features a mechanical quality factor of  $10^7$  due to torsional dissipation dilution.

calibration, and utility in measurement-based feedback cooling of torsional motion.

*High- $Q$  centimeter-scale torsion pendulum.* A remarkable advantage of torsional pendula in studies of gravity is that their suspensions can be realized with exceptionally high mechanical quality factor ( $Q$ ) even when mass-loaded

\* dongchel@mit.edu

† vivishek@mit.edu

[16, 17]. The reason is two-fold [17]: in a doubly-clamped bifilar (or ribbon-shaped) torsional suspension, tensile stress leads to dilution of the intrinsic mechanical dissipation, and the bifilar geometry is naturally soft-clamped so that loss at the clamps, and in the suspended mass, is suppressed. Thus the intrinsic quality factor,  $Q_{\text{int}}$ , is elevated to [17]  $Q_0 = Q_{\text{int}}D_Q$  where the dissipation dilution factor is  $D_Q \approx (\sigma/2E)(w/h)^2$ ; here  $E$  and  $\sigma$  are Young's modulus and tensile stress, and  $w$  and  $h$  are the width and thickness of the ribbon. This is in marked contrast to tensile-stressed mass-loaded linear oscillators, where bending curvature due to the loaded mass [20] erases the advantage from dissipation dilution. This capability positions a macroscopic high- $Q$  torsion pendulum as a unique candidate for both reaching its motional ground state and for gravitational experiments.

We fabricated a doubly-clamped 0.9-cm long thin-film ( $w = 0.5$  mm,  $h = 400$  nm) tensile-stressed ( $\sigma = 0.8$  GPa) torsion pendulum made of stoichiometric  $\text{Si}_3\text{N}_4$ . The device was fabricated starting from a double-sided  $\text{Si}_3\text{N}_4$ -on-Si wafer followed by lithography and reactive ion etching. A second aligned lithography and etch created the window for optical access from the back-side. The device was released using a 24-hour etch in potassium hydroxide. The sample underwent meticulous cleaning with acetone, isopropyl alcohol, deionized water, and oxygen plasma (see SI for more details). The specific device used in the current study has its fundamental torsional mode resonating at  $\Omega_0 = 2\pi \cdot 35.95$  kHz with quality factor  $Q = 1.4 \cdot 10^7$  inferred by ringdown measurements (in vacuum, at  $6 \cdot 10^{-7}$  mbar) as shown in Fig. 1(c). The measured  $Q$  is consistent with the expected dilution factor  $D_Q \approx 2300$ .

*Principle of mirrored optical lever.* To achieve quantum-limited readout of angular motion, we devised a ‘mirrored’ optical lever. Its primary advantage is passive rejection of classical noises arising from the laser beam’s transverse displacement and tilt. Suppose the output of a laser is predominantly in the fundamental Hermite-Gaussian mode with amplitude  $\bar{a} = \sqrt{P/\hbar\omega_\ell}$  ( $P$  the optical power,  $\omega_\ell = 2\pi c/\lambda$  the carrier frequency for a wavelength  $\lambda \approx 1064$  nm), then the optical field can be expressed as [21, 22]  $\hat{E}_{\text{in}}(\mathbf{r}, t) = (\bar{a} + \delta\hat{a}_{00}(t))U_{00}(\mathbf{r}) + \sum_{n,m} \delta\hat{a}_{nm}(t)U_{nm}(\mathbf{r})$ . Here  $U_{nm}(\mathbf{r})$  is the  $(n, m)$ -Hermite-Gaussian ( $\text{HG}_{nm}$ ) basis function (see SI); the operators  $\{\delta\hat{a}_{nm}(t)\}$  represent fluctuations in the laser field, which in the ideal case, when the field is quantum-noise-limited, model the quantum vacuum fluctuations in  $\text{HG}_{nm}$  mode. If this incident field is subjected to a transverse displacement  $\delta\mathbf{r} = (\delta x, 0, 0)$  and angular tilt  $\delta\theta$  at its beam waist, the optical field is transformed to  $\hat{E}_{\text{out}}(\mathbf{r}, t) \approx \hat{E}_{\text{in}}(\mathbf{r}, t) + \bar{a}(\delta x/w_0 + ikw_0\delta\theta/2)U_{10}(\mathbf{r})$ , where  $w_0$  is the waist size. That is, transverse or angular motion scatters light from the incident  $\text{HG}_{00}$  mode to the  $\text{HG}_{10}$  mode in proportion to the motion. When the beam waist is placed at the location of the torsion pendulum, its motion  $\delta\hat{\theta}_{\text{sig}}(t)$  is experienced twice by the reflected optical beam,

i.e.  $2\delta\hat{\theta}_{\text{sig}}(t)$ ; the incident beam may also have extraneous classical noises in the transverse displacement ( $\delta\hat{x}_{\text{ext}}$ ) and tilt ( $\delta\hat{\theta}_{\text{ext}}$ ). When the reflected beam is detected by a split balanced photodetector (SPD) downstream, the resulting photocurrent fluctuations are described by its (symmetrized single-sided) power spectral density (see SI, we neglect correlations between the tilt and transverse displacement [22])

$$S_I[\Omega] = \frac{2}{\pi}(2\eta R P k w_0 \sin \zeta)^2 \left[ S_\theta^{\text{sig}}[\Omega] + \frac{1}{4} S_\theta^{\text{ext}}[\Omega] + \left( \frac{\cot \zeta}{k w_0^2} \right)^2 S_x^{\text{ext}}[\Omega] + \frac{\pi/2}{2\eta(\bar{a} k w_0)^2} \text{csc}^2 \zeta \right], \quad (1)$$

where  $R$  is the responsivity of the detector,  $\eta$  the detection efficiency, and  $\zeta$  is the Gouy phase shift from the torsion pendulum to the SPD. The last three terms represent the imprecision in the measurement arising from extraneous tilt noise ( $S_\theta^{\text{ext}}$ ), extraneous transverse displacement noise ( $S_x^{\text{ext}}$ ), and the fundamental imprecision from quantum vacuum fluctuations (from all odd-order HG modes that the SPD is sensitive to; see SI). Thus, quantum-noise-limited detection of torsional motion is only possible if extraneous noise in the spatial mode of the laser beam is suppressed.

Our mirrored optical lever technique (shown in Fig. 1a,b) cancels classical spatial mode noise to achieve quantum-noise-limited detection. Specifically, the laser beam is split by a polarizing beam splitter (PBS) into two paths: one arm to the torsion pendulum, and the other to a retroreflector. A corner cube retroreflector produces a mirror-image of the laser beam’s transverse displacement and tilt, i.e.  $\delta\hat{a}_{10} \rightarrow -\delta\hat{a}_{10}$  after interacting with the retroreflector (Fig. 1(b)(i) shows the effect of this on input noise), whereas the torsion pendulum induces pure tilt (Fig. 1(b)(ii)). The fields from the two arms are collected by quarter-wave plates at the PBS, and subsequently detected by the SPD with a Gouy phase control using a lens. Careful balancing of the power and Gouy phase in the two arms ensures arbitrarily good cancellation of extraneous noises (acquired by the laser beam before the PBS, Fig. 1(b)(iii)) and transduction of torsional motion into transverse displacement at the SPD (Fig. 1(b)(iv)). Thus, for the mirrored optical lever

$$S_I[\Omega] = \frac{2}{\pi}(2\eta R P k w_0 \sin \zeta)^2 \left[ S_\theta^{\text{sig}}[\Omega] + \frac{\pi/2}{\eta(\bar{a} k w_0)^2} \text{csc}^2 \zeta \right], \quad (2)$$

immune to classical noises and thus quantum-noise-limited in its imprecision (see SI for more details). The trade-off is double the quantum noise from the mirrored beam.

In contrast to interferometric detection of linear motion, our scheme is immune to laser phase noise; yet, the mirrored optical lever is qualitatively similar to homodyne detection: the quantum-noise-limited imprecision decreases inversely with optical power ( $\bar{a} \propto P$ ) and the Gouy phase plays the role of the homodyne angle. We

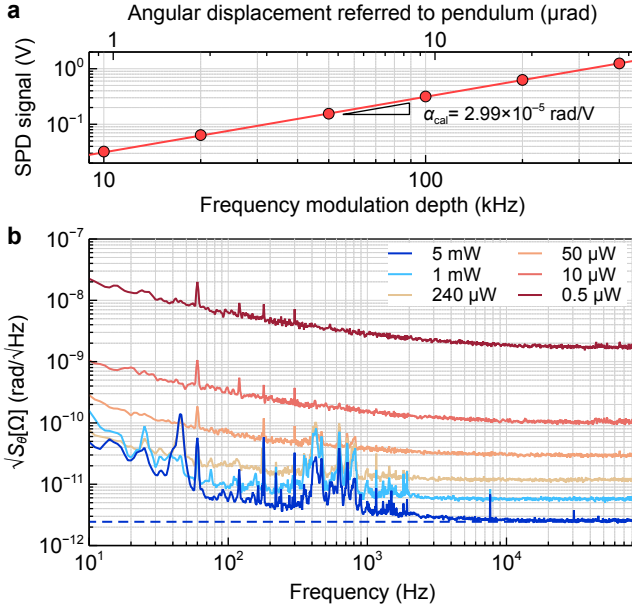


FIG. 2. (a) Calibration curve used to convert the observed SPD signal using the mirrored optical lever to tilt angle at each modulation depth used to drive the AOD (see text for details). (b) Measurement sensitivity of the mirrored optical lever as the optical power is changed. Above 1 kHz, the observed noise is consistent with shot fluctuations arising from quantum noise in the higher-order spatial modes.

place the SPD at Gouy phase  $\zeta = \pi/2$  which maximizes the angular signal.

*Performance and calibration of mirrored optical lever.* In order to investigate the sensitivity of the mirrored optical lever, we first operate it with a flat mirror, instead of the torsion pendulum, in the signal arm.

Independent calibration of the SPD voltage into angular motion is crucial for further investigation. (Note that estimating the angular displacement from the measured optical lever arm does not hold beyond the Rayleigh length.) We perform direct calibration against a known frequency modulation. To wit, an acousto-optic deflector (AOD) is placed at the input plane of the entrance lens of a  $4f$  imaging system (see Fig. 1), with the torsion pendulum (and retroreflector) at the output plane of the second lens. In this configuration, the tilt of the laser beam at the input plane can be modulated by frequency-modulating the AOD drive as  $\Delta\theta_{\text{cal}} = (\lambda/v_c)\Delta f_{\text{cal}}$ , where  $\Delta f_{\text{cal}}$  is the frequency-modulation depth, and  $v_c \approx 5700$  m/s is the acoustic velocity of the AOD quartz crystal. This known tilt change manifests as a voltage change ( $\Delta V_{\text{cal}}$ ) in the SPD signal. By estimating the calibration factor, defined as  $\alpha_{\text{cal}} = \Delta\theta_{\text{cal}}/2\Delta V_{\text{cal}}$ , the angular displacement spectrum is computed from the SPD spectrum:  $S_\theta[\Omega] = \alpha_{\text{cal}}^2 S_V[\Omega]$ , where  $S_V[\Omega]$  is the measured SPD spectrum (see SI for details). Fig. 2(a) shows the voltage amplitude detected by the SPD with different frequency modulation depth of the AOD drive. The beam tilt modulation using the AOM ensures the linear calibration of the voltage to

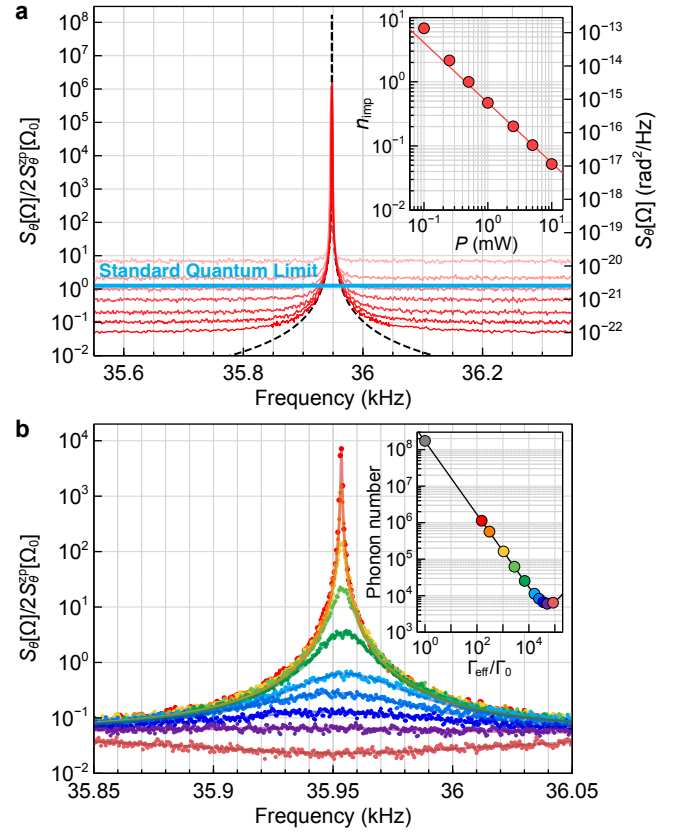


FIG. 3. (a) Thermal Brownian motion of the fundamental torsional mode measured with increasing optical power. Blue shows the resonant standard quantum limit for the measurement of torsional motion. Inset shows the phonon-equivalent imprecision, whose scaling is consistent with quantum-noise-limited detection, and reaches a minimum of  $n_{\text{imp}} \approx 5 \cdot 10^{-2}$ . (b) At the lowest imprecision, the measurement record is used in a feedback loop (see Fig. 1a) to cool the torsional mode via radiation torque to a final phonon occupation of  $n_{\text{eff}} \approx 6 \cdot 10^3$ .

the angular spectrum with an R-square value of 0.99996, as revealed by the linear fit.

Fig. 2(b) demonstrates the calibrated performance of the mirrored optical lever. The angle-referred imprecision noise decreases as the reflected optical power increases, and reaches  $2.6 \cdot 10^{-12}$  rad/ $\sqrt{\text{Hz}}$  with 5 mW incident power, consistent with the quantum-noise scaling in Eq. (2) corresponding to a detection efficiency  $\eta \approx 0.75$ .

The excess noise peaks between 200 Hz and 1 kHz are attributable to seismic noise-induced fluctuations (see SI). Without the mirrored arm, we observed extraneous low frequency tilt noise above 1 mW of optical power that compromised the linearity of the SPD; with the mirrored arm, we characterized input tilt noise suppression by  $\sim 60$  dB over 1 Hz (see SI). Given that our lab temperature is stabilized to a precision around 20 mK [23], we conjecture that the low frequency drifts in input laser tilt are due to refractive index fluctuations from air currents.

*Imprecision below the standard quantum limit.* Next, we place the torsion pendulum in the signal arm of the

mirrored optical lever. Figure 3(a) shows the power spectrum of the measured angular fluctuations of the fundamental torsional mode as the power in the measurement field increases. The observed angle fluctuations  $\delta\hat{\theta}_{\text{obs}} = \delta\hat{\theta}_{\text{phys}} + \delta\hat{\theta}_{\text{imp}}$  consists of the physical motion of the pendulum  $\delta\hat{\theta}_{\text{phys}}$  and the imprecision noise  $\delta\hat{\theta}_{\text{imp}}$  of the optical lever.

The physical motion, shown as the black line in Fig. 3(a), is predominantly due to the thermal Brownian motion of the mode due to its  $n_{\text{th}} = k_B T / (\hbar \Omega_0) \approx 2 \cdot 10^8$  average phonons at room temperature, and is described by the fluctuation-dissipation theorem [24],  $S_{\theta}^{\text{phys}}[\Omega] = 4\hbar(n_{\text{th}} + \frac{1}{2}) \text{Im} \chi_0[\Omega]$ ; here  $\chi_0[\Omega] = [I(-\Omega^2 + \Omega_0^2 + i\Omega\Gamma_0[\Omega])]^{-1}$  is the susceptibility of the torsional mode with moment of inertia  $I$  and damping rate  $\Gamma_0[\Omega] = (\Omega_0/Q)(\Omega_0/\Omega)$ . This model shown as the black line in Fig. 3(a) is based on independent measurement of the frequency, mechanical  $Q$ , and calibrated mode temperature. The latter is inferred by calibrating each spectra using our frequency modulation technique, and assuming that the torsional mode is in thermal equilibrium. We verified (see SI) that the mode temperature is constant across all powers except the highest, which shows a 13% increase, presumably due to optical absorption.

The observed imprecision noise (Fig. 3(a)) is inversely proportional to the optical power, consistent with quantum-noise-limited measurement. The inset shows the measurement imprecision around resonance in equivalent phonon units,  $n_{\text{imp}} = S_{\theta}^{\text{imp}} / 2S_{\theta}^{\text{zp}}[\Omega_0]$ , where  $S_{\theta}^{\text{zp}}[\Omega_0] = 4\theta_{\text{zp}}^2 / \Gamma_0$  is the peak spectral density of the zero-point motion  $\theta_{\text{zp}} = \sqrt{\hbar / (2I\Omega_0)}$  of the torsional mode.

The overall low imprecision of the measurement,  $n_{\text{imp}} \approx 5 \cdot 10^{-2}$ , can be best contextualized by comparing it against the standard quantum limit (SQL). The SQL is the minimum *total* noise in the measurement allowed by quantum mechanics without the use of any quantum enhancement: it is the sum of the zero-point motion of the torsional mode, and the minimum trade-off between the measurement imprecision and the concomitant quantum back-action of the measurement due to quantum fluctuations in the radiation torque of the measurement beam. It can be shown (see SI) that for the measurement scheme we use here, the SQL is given by  $S_{\theta}^{\text{SQL}} = 2S_{\theta}^{\text{zp}}[\Omega_0](1 + \sqrt{\pi})/2 \approx 1.38 \cdot 2S_{\theta}^{\text{zp}}[\Omega_0]$ , which is the blue line in Fig. 3(a). The imprecision in our most precise measurement is  $\sim 13$  dB below the SQL.

*Laser cooling by radiation torque feedback.* The ability to measure with an imprecision below the SQL opens the door for laser cooling of torsional motion, eventually into the ground state, paralleling the development of feedback cooling of linear motion [25–29].

We apply radiation pressure torque ( $\delta\tau_{\text{fb}}$ ) from a second

laser beam, conditioned on the observed motion  $\delta\theta_{\text{obs}}$ , to actuate on the torsional mode. The observed motion is used to synthesize a signal that drives an amplitude modulator in the path of an actuation laser. This beam is focused to a  $50 \mu\text{m}$  spot on the edge of the torsion pendulum (at an angle with respect to the measurement beam so as to not cause scatter into the measurement beam, see Fig. 1(a)). Torque actuation is exclusively driven by radiation pressure and constrained by imprecision noise at the SPD, ensuring that feedback cooling is governed primarily by the observed motion (see SI). The resulting optical feedback torque,  $\delta\tau_{\text{fb}} = -\chi_{\text{fb}}^{-1} \delta\theta_{\text{obs}}$ , can be engineered to affect damping by adjusting the phase of the feedback filter  $\chi_{\text{fb}}^{-1}$  to be  $\pi/2$  around resonance. The low imprecision of the measurement guarantees that the damped motion is in fact cold.

The torsional mode is cooled by increasing the gain in the feedback loop. Figure 3(b) shows the spectrum  $S_{\theta}^{\text{obs}}$  of the observed motion as the gain is increased. The effective damping rates ( $\Gamma_{\text{eff}}$ ) are estimated by fitting the curves to a model of the apparent motion (see SI for details of the model); solid lines show these fits. Assuming that the torsional mode satisfies the equipartition principle, we estimate the phonon occupation from the model of the physical angular motion, using parameters inferred from fits to the observed motion:

$$n_{\text{eff}} \approx \int \frac{S_{\theta}^{\text{phys}} d\Omega}{2\theta_{\text{zp}}^2} \frac{d\Omega}{2\pi} \approx n_{\text{th}} \frac{\Gamma_0}{\Gamma_{\text{eff}}} + n_{\text{imp}} \frac{\Gamma_{\text{eff}}}{\Gamma_0}. \quad (3)$$

The inset in Fig. 3(b) shows the inferred phonon occupation as the effective damping rate is increased by the feedback gain. Feedback cooling cools the torsional mode from an average phonon occupation of  $\sim 2 \cdot 10^8$  (at room temperature) to about  $5964 \pm 39$ , ultimately limited by heating by feedback of imprecision noise, consistent with Eq. (3). This sets the limit  $n_{\text{eff}} \gtrsim 2\sqrt{n_{\text{th}} n_{\text{imp}}}$ .

*Conclusion.* We demonstrated laser cooling of a centimeter-scale torsion pendulum using a measurement whose imprecision is 13 dB below the standard quantum limit. The performance of cooling is limited by the achievable strength of the measurement given the size of the zero-point motion. This limitation can be overcome using lower frequency torsional oscillators laser-cooled in a strong optical trap [30], for which the requirements are much reduced [31] compared to the current protocol. Thus, our work opens the door for eventual quantum state control of macroscopic torsional pendula. Combined with the pedigree and advantage of torsional pendula in the measurement of weak gravitational interactions, this work establishes the necessary step towards mechanical experiments that explore the fundamental nature of gravity.

[1] C.-A. Coulomb, Second mémoire sur l'électricité et le magnétisme, Histoire de l'Académie Royale des Sciences ,

569 (1785).

[2] G. T. Gillies and R. C. Ritter, Torsion balances, tor-

- sion pendulums, and related devices, *Review of Scientific Instruments* **64**, 283 (1993).
- [3] H. Cavendish, Experiments to Determine the Density of the Earth, *Philosophical Transactions of the Royal Society of London* **88**, 469 (1798).
  - [4] E. G. Adelberger, B. R. Heckel, and A. R. Nelson, Tests of the gravitational inverse-square law, *Annual Review of Nuclear and Particle Physics* **53**, 77 (2003).
  - [5] E. G. Adelberger, J. H. Gundlach, B. R. Heckel, S. Hoedl, and S. Schlamminger, Torsion balance experiments: A low-energy frontier of particle physics, *Progress in Particle and Nuclear Physics* **62**, 102 (2009).
  - [6] C. Speake and T. Quinn, The search for Newton's constant, *Physics Today* **67**, 27 (2014).
  - [7] C. Rothleitner and S. Schlamminger, Invited Review Article: Measurements of the Newtonian constant of gravitation, *Review of Scientific Instruments* **88**, 111101 (2017).
  - [8] R. H. Dicke, The Eötvös Experiment, *Scientific American* **205**, 84 (1961).
  - [9] V. B. Braginsky and V. Panov, Verification of the Equivalence of Inertial and Gravitational Mass, *Soviet Physics JETP* **34**, 463 (1972).
  - [10] S. Schlamminger, K.-Y. Choi, T. A. Wagner, J. H. Gundlach, and E. G. Adelberger, Test of the Equivalence Principle Using a Rotating Torsion Balance, *Physical Review Letters* **100**, 041101 (2008).
  - [11] T. A. Wagner, S. Schlamminger, J. H. Gundlach, and E. G. Adelberger, Torsion-balance tests of the weak equivalence principle, *Classical and Quantum Gravity* **29**, 184002 (2012).
  - [12] R. A. Beth, Mechanical detection and measurement of the angular momentum of light, *Physical Review* **50**, 115 (1936).
  - [13] A. Datta and H. Miao, Signatures of the quantum nature of gravity in the differential motion of two masses, *Quantum Science and Technology* **6**, 045014 (2021).
  - [14] L. Lami, J. S. Pedernales, and M. B. Plenio, Testing the Quantumness of Gravity without Entanglement, *Physical Review X* **14**, 021022 (2024).
  - [15] S. Kryhin and V. Sudhir, Distinguishable consequence of classical gravity on quantum matter, [arXiv:2309.09105](https://arxiv.org/abs/2309.09105) (2023).
  - [16] T. J. Quinn, C. C. Speake, and R. S. Davis, Novel torsion balance for the measurement of the Newtonian gravitational constant, *Metrologia* **34**, 245 (1997).
  - [17] J. Pratt, A. Agrawal, C. Condos, C. Pluchar, S. Schlamminger, and D. Wilson, Nanoscale Torsional Dissipation Dilution for Quantum Experiments and Precision Measurement, *Physical Review X* **13**, 011018 (2023).
  - [18] T. Westphal, H. Hepach, J. Pfaff, and M. Aspelmeyer, Measurement of gravitational coupling between millimetre-sized masses, *Nature* **591**, 225 (2021).
  - [19] M. Aspelmeyer, T. J. Kippenberg, and F. Marquardt, Cavity optomechanics, *Rev. Mod. Phys.* **86**, 1391 (2014).
  - [20] R. Shaniv, S. K. Keshava, C. Reetz, and C. A. Regal, Understanding the quality factor of mass-loaded tensioned resonators, *Physical Review Applied* **19**, L031006 (2023).
  - [21] Y. Enomoto, K. Nagano, and S. Kawamura, Standard quantum limit of angular motion of a suspended mirror and homodyne detection of a ponderomotively squeezed vacuum field, *Physical Review A* **94**, 012115 (2016).
  - [22] S. Hao and T. P. Purdy, Back action evasion in optical lever detection, *Optica* **11**, 10 (2024).
  - [23] D. S. Fife, D.-C. Shin, and V. Sudhir, Temperature stabilization of a lab space at 10mk-level over a day, [arXiv:2404.07101](https://arxiv.org/abs/2404.07101) (2024).
  - [24] H. Callen and T. Welton, Irreversibility and generalized noise, *Physical Review* **83**, 34 (1951).
  - [25] J. Courty, A. Heidmann, and M. Pinard, Quantum limits of cold damping with optomechanical coupling, *European Physical Journal D* **17**, 399 (2001).
  - [26] D. J. Wilson, V. Sudhir, N. Piro, R. Schilling, A. Ghadimi, and T. J. Kippenberg, Measurement-based control of a mechanical oscillator at its thermal decoherence rate, *Nature* **524**, 325 (2015).
  - [27] M. Rossi, D. Mason, J. Chen, Y. Tsaturyan, and A. Schliesser, Measurement-based quantum control of mechanical motion, *Nature* **563**, 53 (2018).
  - [28] L. Magrini, P. Rosenzweig, C. Bach, A. Deutschmann-Olek, S. G. Hofer, S. Hong, N. Kiesel, A. Kugi, and M. Aspelmeyer, Real-time optimal quantum control of mechanical motion at room temperature, *Nature* **595**, 373 (2021).
  - [29] F. Tebbenjohanns, M. L. Mattana, M. Rossi, M. Frimmer, and L. Novotny, Quantum control of a nanoparticle optically levitated in cryogenic free space, *Nature* **595**, 378 (2021).
  - [30] C. Whittle, E. D. Hall, S. Dwyer, N. Mavalvala, V. Sudhir, and LIGO Instrument Science Group, Approaching the motional ground state of a 10-kg object, *Science* **372**, 1333 (2021).
  - [31] K. Komori, D. Ďurovčíková, and V. Sudhir, Quantum theory of feedback cooling of an anelastic macromechanical oscillator, *Physical Review A* **105**, 043520 (2022).
  - [32] A. E. Siegman, *Lasers* (University Science Books, 1986).
  - [33] A. Wünsche, Quantization of Gauss-Hermite and Gauss-Laguerre beams in free space, *Journal of Optics B: Quantum and Semiclassical Optics* **6**, S47 (2004).
  - [34] C. H. Metzger and K. Karrai, Cavity cooling of a microlever., *Nature* **432**, 1002 (2004).
  - [35] D. Kleckner and D. Bouwmeester, Sub-kelvin optical cooling of a micromechanical resonator., *Nature* **444**, 75 (2006).
  - [36] A. Schliesser, P. Del'Haye, N. Nooshi, K. Vahala, and T. Kippenberg, Radiation Pressure Cooling of a Micromechanical Oscillator Using Dynamical Backaction, *Physical Review Letters* **97**, 243905 (2006).
  - [37] V. Sudhir, *Quantum limits on measurement and control of a mechanical oscillator* (Springer, 2017).

## Supplementary Information

### CONTENTS

A. Torsion pendulum	6
1. Fabrication	6
2. Ringdown measurements	7
B. Noise in an optical lever	7
1. Measurement imprecision in split photo-detected optical lever	8
2. Measurement back action in optical lever	9
3. Total measurement noise and the Standard Quantum Limit	10
C. Extraneous noise cancellation in mirrored optical lever	10
D. Angle calibration	12
1. Calibration of mirrored optical lever	12
2. Calibration of thermal noise spectra	13
E. Measurement-based feedback cooling	14
1. Theory	14
2. Implementation of feedback	15
3. Extraneous noise in feedback	15
4. Estimation of mode temperature	16

### Appendix A: Torsion pendulum

#### 1. Fabrication

The torsion pendulum used in this work is fabricated starting with a double-sided, 400 nm thick  $\text{Si}_3\text{N}_4$ -on-Si wafer (WaferPro); Fig. 4 shows the essential steps in the process. We coated both sides with  $3\ \mu\text{m}$  thick S1813 positive photoresist. Using mask lithography, we patterned the top-side resist with the pendulum shape, while the bottom-side resist protected the wafer from scratches during handling. We transferred the pattern to the SiN film using a  $\text{CF}_4$ -based reactive ion etch. After removing the remaining photoresist, we applied a fresh coat to both sides. We then patterned the backside with a square window, carefully aligning it with the front pattern. After dry-etching the square window into the wafer, we applied a thick layer of photoresist to both sides for protection. We diced the wafer into individual samples. We removed the photoresist using an acetone, iso-propyl alcohol (IPA), and de-ionized (DI) water rinse, followed by an oxygen plasma clean to eliminate any lingering residue. We vertically placed each sample in a  $74^\circ\text{C}$  potassium hydroxide bath for 24 hours. After etching, we rinsed the samples in DI water, followed by IPA, and let them air-dry. Finally, we gave the device a final oxygen plasma clean to remove any remaining residue.

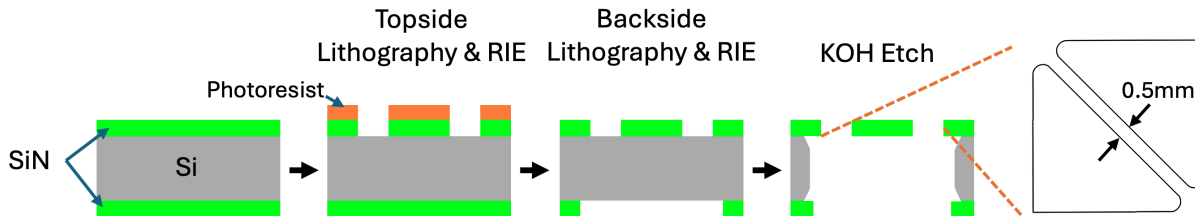


FIG. 4. Essential steps in the process flow for fabricating the torsion pendulum.

## 2. Ringdown measurements

The mechanical Q of the fundamental torsional mode was estimated from ringdown measurements. The motion is excited by a radiation pressure torque, and measured using the SPD. The measured signal is demodulated at the mechanical frequency using a lock-in amplifier (Moku:Pro, Liquid Instruments). Figure 5 shows such measurements at a few different powers of the measurement beam.

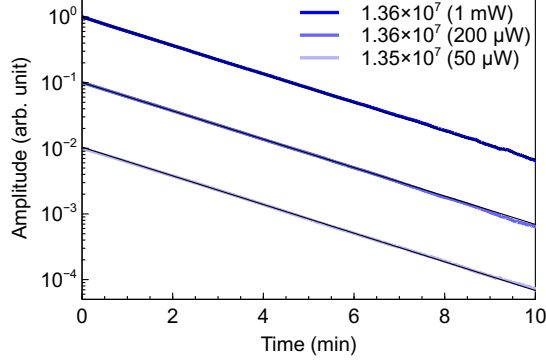


FIG. 5. Ringdown measurements of the fundamental torsion mode at  $\Omega_0/2\pi = 35.95\text{kHz}$  with different probe beam powers

### Appendix B: Noise in an optical lever

To better understand the quantum noises in optical lever detection, we consider here the decomposition of a quantized optical field on an orthonormal Hermite-Gaussian (HG) basis. The HG mode  $U_{mn}$  of  $m$ -th order in x-axis and  $n$ -th order in y-axis is defined as [32, §16.4]

$$U_{mn}(x, y, z, t) = u_{mn}(x, y, z) e^{i\phi_{mn}(x, y, z, t)}, \quad (\text{B1})$$

$$u_{mn}(x, y, z) = \sqrt{\frac{2}{\pi}} \frac{1}{w(z)} \frac{1}{\sqrt{2^{m+n} m! n!}} e^{-(x^2+y^2)/w^2(z)} H_m(\sqrt{2}x/w(z)) H_n(\sqrt{2}y/w(z)), \quad (\text{B2})$$

$$\phi_{mn}(x, y, z, t) = \omega_\ell t - kz - \frac{k(x^2 + y^2)}{2R(z)} + (m + n + 1)\zeta(z); \quad (\text{B3})$$

here,  $\omega_\ell$  and  $k$  are the angular frequency and wavenumber of the laser beam;  $w(z) = w_0 \sqrt{1 + (z/z_R)^2}$ ,  $R(z) = z(1 + (z_R/z)^2)$ , and  $\zeta(z) = \text{artan}(z/z_R)$  are the beam radius, radius of curvature, and Gouy phase, respectively;  $w_0$  is the beam width at the waist;  $z_R = kw_0^2/2$  is the Rayleigh length; and  $H_n$  is the  $n^{\text{th}}$  Hermite polynomial. These bases satisfy the orthonormality relation  $\int dx dy U_{mn}^* U_{m'n'} = \delta_{mm'} \delta_{nn'}$ .

The quantized electric field (in an arbitrary, but static polarization direction) of a laser beam with power  $P$  in the (fundamental) HG<sub>00</sub> mode — such as the emission of an ideal laser — can be modeled by

$$\hat{E}(x, y, z, t) = (\bar{a} + \delta\hat{a}_{00}(t))U_{00} + \sum_{mn} \delta\hat{a}_{mn}(t)U_{mn}. \quad (\text{B4})$$

Here  $\bar{a} = \sqrt{P/\hbar\omega_\ell}$  is the mean photon flux amplitude and the operators  $\delta\hat{a}_{mn}$  represent fluctuations in  $U_{mn}$  mode, that satisfy the canonical commutation relations [33]:

$$[\delta\hat{a}_{mn}[\Omega], \delta\hat{a}_{m'n'}[\Omega']^\dagger] = 2\pi\delta_{mm'}\delta_{nn'}\delta[\Omega + \Omega']. \quad (\text{B5})$$

In the ideal case, the fluctuations are given by vacuum fluctuations of the HG modes,  $\delta\hat{a}_{mn}^0$ , derived through the projection of the fluctuations of a plane wave into the HG modes. To account for extraneous transverse displacement and tilt noises, we set

$$\delta\hat{a}_{mn} = \delta\hat{a}_{mn}^0 + \delta a_{mn}^{\text{ext}}, \quad (\text{B6})$$

where  $\delta a_{mn}^{\text{ext}}$  represent the extraneous fluctuations in each mode.

Let us consider a case where the laser beam at arbitrary point  $z = Z$  is transversely displaced by  $\delta x$  and tilted by  $\delta\theta$  in the  $xz$  plane, viz.,

$$\hat{E}(x, y, Z, t) \rightarrow \hat{E}(x - \delta x, y, Z, t)e^{ik\delta\theta x} \approx \hat{E}(x, y, Z, t) + \bar{a} \left( \frac{1}{w(Z)}\delta\hat{x} + i\frac{kw(Z)}{2}\delta\hat{\theta} \right) e^{-i\zeta(Z)}U_{10}, \quad (\text{B7})$$

where we assume  $\delta x, \delta\theta \ll 1$ , and have then represented these fluctuations by associating them with operators. Eq. (B7) shows that the laser beam's transverse displacement and tilt can be interpreted as the scattering of the fundamental mode to the first-order mode. For instance, at the beam waist ( $z = 0$ ), the displacement (tilt) fluctuations are encoded into the amplitude (phase) quadrature of the first-order mode, while in the far field ( $z \ll z_0$  or  $z \ll -z_0$ ) the fluctuations are transposed to the opposite quadratures. Meanwhile, Eq. (B7) also explicitly shows how the first-order amplitude and phase quadratures contribute to the displacement and tilt fluctuations along the beam propagation:

$$\delta\hat{x}(Z) = \frac{w(Z)}{2\bar{a}}(\delta\hat{a}_{10}e^{i\zeta(Z)} + \delta\hat{a}_{10}^\dagger e^{-i\zeta(Z)}) \quad (\text{B8})$$

$$\delta\hat{\theta}(Z) = \frac{1}{i\bar{a}kw(Z)}(\delta\hat{a}_{10}e^{i\zeta(Z)} - \delta\hat{a}_{10}^\dagger e^{-i\zeta(Z)}) \quad (\text{B9})$$

This represents the essence of the optical lever technique; the laser tilt produced by a torsion pendulum at the beam waist is converted into the transverse displacement at the far field.

### 1. Measurement imprecision in split photo-detected optical lever

Thus, a split photodetector (SPD) can be used in the far field to detect the transverse displacement of the laser beam, and thereby infer the tilt that produced it [21, 22]. Specifically, the SPD takes the difference of the photocurrents from a pair of photodetectors placed next to each other, which we take to be horizontal in the plane perpendicular to the propagation direction  $z$ . The photocurrent operator  $\hat{I}(t; z)$  for the SPD located at a distance  $z$  can be computed by the photon number operator,  $\hat{n} = \hat{a}^\dagger \hat{a}$ , as

$$\begin{aligned} \hat{I}(t; z) &= q_e [\hat{n}_R(t) - \hat{n}_L(t)] \\ &= q_e \int_{-\infty}^{\infty} dx \int_{-\infty}^{\infty} dy \operatorname{sgn}(x) \hat{E}^\dagger(x, y, z, t) \hat{E}(x, y, z, t) \\ &= 2q_e \bar{a} \sum_{m, n \neq 0} \frac{1}{\sqrt{2^{m+n} m! n!}} \operatorname{Re} \left[ \delta\hat{a}_{mn}(t) e^{i(m+n)\zeta(z)} \right] \int_{-\infty}^{\infty} dx \operatorname{sgn}(x) \int_{-\infty}^{\infty} dy \frac{2}{\pi w(z)^2} H_m(x) H_n(y) e^{-\frac{2(x^2+y^2)}{w(z)^2}} \\ &= \frac{2}{\pi} q_e \bar{a} \sum_{m, n \neq 0} \frac{1}{\sqrt{2^{m+n} m! n!}} \operatorname{Re} \left[ \delta\hat{a}_{mn}(t) e^{i(m+n)\zeta(z)} \right] \int_{-\infty}^{\infty} dx \operatorname{sgn}(x) H_m(x) e^{-x^2} \int_{-\infty}^{\infty} dy H_n(y) e^{-y^2} \\ &= 2q_e \bar{a} \sum_{m \neq 0} \frac{1}{\sqrt{\pi 2^m m!}} \operatorname{Re} [\delta\hat{a}_{m,0}(t) e^{im\zeta(z)}] \int_0^{\infty} dx (1 - (-1)^m) H_m(x) e^{-x^2} \\ &= 4q_e \bar{a} \sum_{k=0}^{\infty} \frac{1}{\sqrt{\pi 2^{2k+1} (2k+1)!}} \operatorname{Re} [\delta\hat{a}_{2k+1,0}(t) e^{i(2k+1)\zeta(z)}] \int_0^{\infty} dx H_{2k+1}(x) e^{-x^2} \\ &= 4q_e \bar{a} \sum_{k=0}^{\infty} \operatorname{Re} [\delta\hat{a}_{2k+1,0}(t) e^{i(2k+1)\zeta(z)}] \frac{(-1)^k}{(2k+1)k!} \sqrt{\frac{(2k+1)!}{\pi 2^{2k+1}}} \\ &= \frac{2}{\sqrt{\pi}} q_e \bar{a} \sum_{k=0}^{\infty} [\delta\hat{q}_{2k+1,0}(t) \cos((2k+1)\zeta(z)) - \delta\hat{p}_{2k+1,0}(t) \sin((2k+1)\zeta(z))] D_k \end{aligned} \quad (\text{B10})$$

where  $q_e$  is the electron charge,  $\delta\hat{q}_{mn}(t) = (\delta\hat{a}_{mn} + \delta\hat{a}_{mn}^\dagger)/\sqrt{2}$  and  $\delta\hat{p}_{mn}(t) = (\delta\hat{a}_{mn} - \delta\hat{a}_{mn}^\dagger)/\sqrt{2}i$  are amplitude and phase quadrature operators, and the coefficient  $D_k$  is defined as  $D_k = \frac{(-1)^k}{(2k+1)k!} \sqrt{\frac{(2k+1)!}{\pi 2^{2k+1}}}$ . Eq. (B10) shows that the split photodetection leads to the detection of quadratures of the odd-number HG modes  $\delta\hat{a}_{2k+1,0}$ , being amplified by



the amplitude  $\bar{a}$  of the fundamental HG mode, and with a rotation determined by the Gouy phase acquired during propagation. That is, in analogy with a balanced homodyne detection employed for measurement of longitudinal phase fluctuations, the amplitude of fundamental mode  $\bar{a}$  and the Gouy phase shift act as the local oscillator beam and the homodyne angle, respectively.

Suppose now that the angular fluctuations are produced by the motion of a torsion pendulum positioned at  $z = z_0$ . The laser beam reflected off from the torsion pendulum, whose angular motion is denoted as  $\delta\hat{\theta}_{\text{sig}}$ , attains a tilt of  $2\delta\hat{\theta}_{\text{sig}}$ . Given that the laser beam is subject to extraneous classical noises in the first-order HG mode, i.e. classical transverse displacement ( $\delta\hat{x}_{\text{ext}}$ ) and tilt noise ( $\delta\hat{\theta}_{\text{ext}}$ ) referred to the position of the torsion pendulum, the optical field can be expressed as

$$\hat{E}(\mathbf{r}, t) \approx \bar{a}U_{00}(\mathbf{r}, t) + \left[ \frac{\bar{a}}{w(z_0)}\delta\hat{x}_{\text{ext}} + i\frac{kw(z_0)}{2}(2\delta\hat{\theta}_{\text{sig}} + \delta\hat{\theta}_{\text{ext}}) \right] U_{10}(\mathbf{r}, t) + \sum_{n,m} \delta\hat{a}_{nm}(t)U_{nm}(\mathbf{r}, t). \quad (\text{B11})$$

Then, the symmetrized single-sided spectral density of the photocurrent can be computed from Eq. (B10) as

$$S_I[\Omega] = \frac{2}{\pi}(2\eta R P k w(z_0) \sin \zeta)^2 \left[ S_{\theta}^{\text{sig}}[\Omega] + \frac{1}{4}S_{\theta}^{\text{ext}}[\Omega] + \left( \frac{\cot \zeta}{kw(z_0)^2} \right)^2 S_x^{\text{ext}}[\Omega] + \frac{\pi/2}{2\eta(\bar{a}kw(z_0))^2} \csc^2 \zeta \right], \quad (\text{B12})$$

where  $R = q_e/\hbar w_l$  and  $\eta$  are the responsivity and the quantum efficiency of the SPD, and  $\zeta = \zeta(z) - \zeta(z_0)$  is the Gouy phase shift from the torsion pendulum to the SPD. In this calculation, the single-sided spectral densities of the vacuum fluctuations are  $S_q^{mn,0} = 1$  and  $S_p^{mn,0} = 1$  (Eq. (B5)), and  $\sum_{k=0}^{\infty} D_k^2 = \pi/2$ . Note that transduction of angular motion to SPD signal reaches its maximum value when the Gouy phase shift is set to  $\pi/2$ . This condition can be achieved either by preparing a sufficient lever length, i.e.,  $z - z_0 \gg z_R$ , or by controlling the accumulated Gouy phase shift with a lens. The last term in Eq. (B12) gives the imprecision noise due to quantum fluctuations in the higher-order modes,

$$S_{\theta}^{\text{imp}}[\Omega] = \frac{\pi/2}{2\eta(\bar{a}kw(z_0))^2} \csc^2 \zeta, \quad (\text{B13})$$

whereas the second and third terms represent the imprecision noise from extraneous fluctuations in the laser.

## 2. Measurement back action in optical lever

We consider the quantum back-action torque induced by the laser beam in the optical lever. In the main manuscript, it is assumed that the laser beam is incident at the center of the torsion pendulum. Here, we address the scenario where the laser beam is offset by a distance  $x_0$  from the center of rotation of the torsion pendulum. By linearizing the torque fluctuations, the back-action torque can be expressed as

$$\delta\hat{\tau}_{\text{ba}}[\Omega] = F\delta\hat{x}[\Omega] + \delta\hat{F}[\Omega]x_0, \quad (\text{B14})$$

where the first term represents the back-action torque due to the transverse displacement fluctuation, and the second term accounts for the force fluctuation. The spectral density of the back-action torque is given by

$$S_{\tau}^{\text{ba}}[\Omega] = F^2 S_x[\Omega] + x_0^2 S_F[\Omega]. \quad (\text{B15})$$

In general, these fluctuations can be decomposed into two contributions: extraneous classical noise and quantum noise. Therefore, we incorporate the classical components of the fluctuations, denoted as  $S_x^{\text{ext}}[\Omega]$  and  $S_F^{\text{ext}}[\Omega]$ . The quantum fluctuation of the transverse displacement can be derived from Eq.(B8) as  $S_x[\Omega] = w^2(z_0)/2\bar{a}^2$ , while the quantum radiation pressure force fluctuation is given by  $S_F^{\text{ba}}[\Omega] = 8\bar{a}^2\hbar^2k^2$ , with the mean radiation pressure force  $F_{\text{ba}} = 2\bar{a}^2\hbar^2k^2$ . Consequently, the total back-action torque is expressed as

$$S_{\tau}^{\text{ba}}[\Omega] = (\sqrt{2}\hbar\bar{a}kw(z_0))^2 \left[ 1 + \left( \frac{2x_0}{w(z_0)} \right)^2 \right] + (2\hbar\bar{a}^2k)^2 S_x^{\text{ext}} + x_0^2 S_F^{\text{ext}}. \quad (\text{B16})$$

The first term arises from quantum fluctuations in the optical beam used for the measurement (with the term  $\propto x_0$  coming from any potential mis-centering of the beam on the torsion pendulum), while the second and third terms arise from extraneous fluctuations in it.

### 3. Total measurement noise and the Standard Quantum Limit

The observed SPD signal, referred to angle, can be understood as the sum of the intrinsic (i.e. thermal and zero-point) motion, back-action-driven motion, and measurement imprecision, i.e.

$$\delta\hat{\theta}_{\text{obs}} = \delta\hat{\theta}_{\text{int}} + \delta\hat{\theta}_{\text{ba}} + \delta\hat{\theta}_{\text{imp}}. \quad (\text{B17})$$

The intrinsic motion is given by the fluctuation-dissipation theorem [24]

$$S_{\theta}^{\text{int}}[\Omega] = 4\hbar(n_{\text{th}}[\Omega] + \frac{1}{2}) \text{Im} \chi_0[\Omega], \quad (\text{B18})$$

where  $n_{\text{th}}[\Omega] = (e^{\hbar\Omega/k_B T} - 1)^{-1}$  is the average thermal phonon occupation at temperature  $T$ , and  $\chi_0[\Omega] = [I(-\Omega^2 + \Omega_0^2 - i\Omega\Gamma_0[\Omega])]^{-1}$  is the mechanical susceptibility for the torsion pendulum with moment of inertia  $I$  and frequency-dependent structural damping rate  $\Gamma_0[\Omega] = (\Omega_0/Q)(\Omega_0/\Omega)$ . The back-action-driven motion is  $\delta\hat{\theta}_{\text{ba}} = \chi_0\delta\tau_{\text{ba}}$ , whose spectrum is

$$S_{\theta}^{\text{ba}} = |\chi_0|^2 S_{\tau}^{\text{ba}}, \quad (\text{B19})$$

with  $S_{\tau}^{\text{ba}}$  given by Eq. (B16).

Note from Eqs. (B16) and (C3) that as the measurement imprecision due to quantum noise decreases ( $\propto 1/P$ ), quantum back-action increases ( $\propto P$ ). Thus the measured angular noise has a minimum

$$S_{\theta}^{\text{obs}} = S_{\theta}^{\text{int}} + S_{\theta}^{\text{ba}} + S_{\theta}^{\text{imp}} \geq S_{\theta}^{\text{int}} + 2\sqrt{S_{\theta}^{\text{ba}} S_{\theta}^{\text{imp}}}, \quad (\text{B20})$$

whose ideal limit (zero temperature, perfect detection efficiency, beam perfectly centered, no extraneous imprecision or back-action) on resonance defines the (resonant) standard quantum limit (SQL) of the measurement:

$$S_{\theta}^{\text{SQL}}[\Omega_0] = 2\hbar \text{Im} \chi_0[\Omega_0](1 + \sqrt{\pi}) = 2S_{\theta}^{\text{zp}}[\Omega_0] \frac{1 + \sqrt{\pi}}{2}. \quad (\text{B21})$$

Here the spectral density of the zero-point motion of the torsional mode is

$$S_{\theta}^{\text{zp}}[\Omega_0] = S_{\theta}^{\text{int}}[\Omega_0]|_{T=0} = \frac{4\theta_{\text{zp}}^2}{\Gamma_0}, \quad (\text{B22})$$

where  $\theta_{\text{zp}} = \sqrt{\hbar/(2I\Omega_0)}$  is the zero-point motion of the mode. In contrast to the SQL for the measurement of linear motion, this is larger than twice the resonant zero-point motion of the mechanical oscillator by  $(1 + \sqrt{\pi})/2 \approx 1.386$ .

### Appendix C: Extraneous noise cancellation in mirrored optical lever

Here we describe the noise spectral density in the mirrored optical lever. In this configuration (as shown in Fig. 1 in the main text), the input laser beam is prepared to have equal components for polarizations in S and P, so that the P-polarized component passes on to the torsion pendulum to sense the angular motion (signal arm), while the S-polarized component is diverted to a retroreflector (reference arm). A retroreflector is a  $90^\circ$  corner cube that inverts the tilt and transverse displacement of the beam with respect to the normal reflection from a flat mirror, i.e., it alters the sign of the amplitude flux of the first-order HG mode as  $\delta\hat{a}_{10}(t) \rightarrow -\delta\hat{a}_{10}(t)$ . In each arm, a quarter-wave plate is positioned so that both beams are collected from the output port of the PBS. The output optical field is written as  $\hat{\mathbf{E}}_{\text{out}}(\mathbf{r}, t) = \hat{\mathbf{E}}_{\text{sig}}(\mathbf{r}, t)\mathbf{e}_S + \hat{\mathbf{E}}_{\text{ref}}(\mathbf{r}, t)\mathbf{e}_P$ , where  $\mathbf{e}_S$  and  $\mathbf{e}_P$  are the unit vectors for S and P polarizations, respectively. The signal and reference fields are obtained from the Eq.(B7) as

$$\hat{\mathbf{E}}_{\text{sig}}(\mathbf{r}, t) = \bar{a}U_{00}^{\text{sig}}(\mathbf{r}, t) + \left[ \frac{\bar{a}}{w(z_0)}\delta\hat{x}_{\text{ext}} + i\frac{kw(z_0)}{2}(2\delta\hat{\theta}_{\text{sig}} + \delta\hat{\theta}_{\text{ext}}) \right] U_{10}^{\text{sig}}(\mathbf{r}, t) + \sum_{n,m} \delta\hat{a}_{nm}(t)U_{nm}^{\text{sig}}(\mathbf{r}, t), \quad (\text{C1})$$

$$\hat{\mathbf{E}}_{\text{ref}}(\mathbf{r}, t) = \bar{a}U_{00}^{\text{ref}}(\mathbf{r}, t) + \left[ -\frac{\bar{a}}{w(z_0)}\delta\hat{x}_{\text{ext}} - i\frac{kw(z_0)}{2}\delta\hat{\theta}_{\text{ext}} \right] U_{10}^{\text{ref}}(\mathbf{r}, t) + \sum_{n,m} \delta\hat{a}_{nm}(t)U_{nm}^{\text{ref}}(\mathbf{r}, t). \quad (\text{C2})$$

Here,  $U_{mn}^{\text{sig(ref)}}$  represents the notation for the HG modes coming from the signal (reference) arm. We assume that the optical power and arm length for each arm are identical. The combined field is then detected by an SPD, yielding the photocurrent density as

$$S_I[\Omega] = \frac{2}{\pi}(2\eta R P k w(z_0) \sin \zeta)^2 \left[ S_{\theta}^{\text{sig}}[\Omega] + \frac{\pi/2}{\eta(\bar{a}kw_0)^2} \csc^2 \zeta \right], \quad (\text{C3})$$

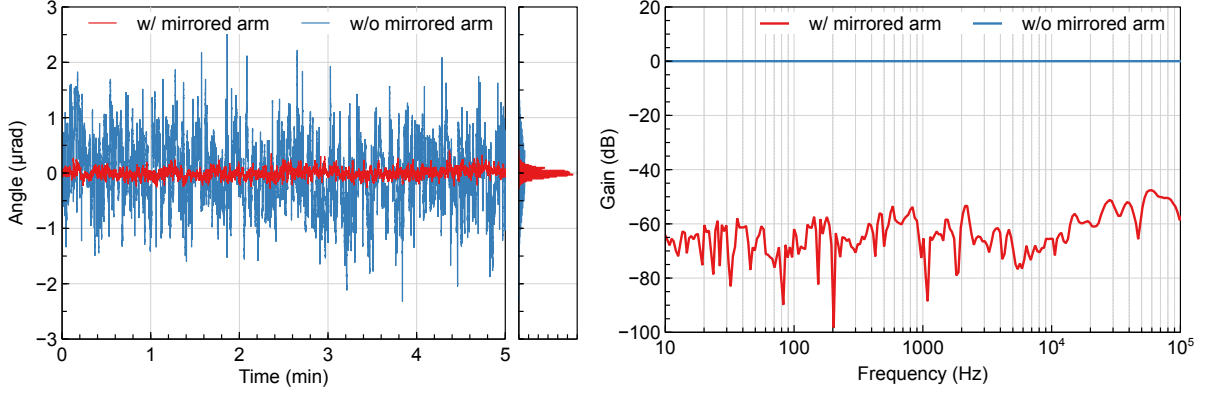


FIG. 6. Characterization of the mirrored optical lever. (a) Ambient angle fluctuation over time with and without the mirrored arm. (b) Frequency response measurement. A sinusoidal tilt modulation is produced by the acousto-optic deflector and measured by the split photodetector, followed by a lock-in amplification to measure the gain between the input and output signals. The response gain is normalized by the gain without the mirrored arm.

This indicates that the reference beam cancels out the classical displacement and tilt noises with the trade-off of the doubled shot noise. The orthogonal polarizations for the optical fields allow us to obviate the requirement for stabilizing laser frequency noise. The sensitivity for the angular motion detection is maximized when the Gouy phase shift  $\zeta$  is precisely set to  $\pi/2$  as follows:

$$S_I[\Omega] = \frac{2}{\pi} (2\eta R P k w(z_0))^2 \left[ S_{\theta}^{\text{sig}}[\Omega] + \frac{\pi/2}{\eta(\bar{a} k w(z_0))^2} \right], \quad (\text{C4})$$

This result shows that, in principle, the mirrored optical lever with the use of a retroreflector is immune to the classical noises that the laser beam experiences before the PBS.

In our experiment, the output laser beam is split by a knife-edge right-angle mirror and then collected by a low noise balanced photodetector (HBPR-100M-60K-IN-FS, Femto). The difference in photocurrents between the two photodiodes of the BPD corresponds to the transverse displacement of the laser beam at the knife-edge mirror. The Gouy phase shift in Eq. (C3) is defined by the locations of the torsion pendulum and knife-edge mirror. We set the Gouy phase to be  $\pi/2$  by manipulating a lens between the torsion pendulum and the knife-edge mirror.

To characterize the classical noise suppression of the mirrored optical lever, we measure the angular fluctuations over time with and without the mirrored arm. In this proof-of-concept experiment, the torsion pendulum is replaced with a flat mirror so that the performance is only limited by the measurement system. Fig. 6(a) shows the angle fluctuations of the laser beam referred to the location of the flat mirror over 300 s with a sampling rate of 100 Hz. We observe that the tilt fluctuation (blue curve) is suppressed when the mirrored image is simultaneously incident on the SPD, reducing the standard deviation from 620 nrad to 73 nrad. Furthermore, we characterize the mirrored optical lever system in terms of the frequency response. To this end, we generate the periodic virtual tilt signal swept over 1 Hz – 100 kHz using the acousto-optic deflector. This virtual angular signal is detected by the SPD and subsequently lock-in amplified. As shown in Fig. 6(b), we confirm that the mirrored optical lever is capable of reducing the angle fluctuations by 50–60 dB in a broad frequency range up to 100 kHz. Thine residual noise may be due to the imperfect polarization division, the finite extinction ratio of the PBS  $\sim 3000$ , and other systematic errors.

In Fig. 2(a) of the main text, excess noise is observed in the low-frequency regime below 1 kHz Fourier frequency. Potential sources of this extraneous noise include seismic noise and residual spatial noise caused by air current-induced refractive index fluctuations. (Laser intensity noise is significantly suppressed by balanced photodetection at the SPD, and the optical lever is insensitive to the phase quadrature of the laser beam.) To elucidate the origins of this excess noise, we examine the coherence spectrum between the angular displacement noise  $S_{\theta}[\Omega]$  and seismic displacement noise  $S_x^{\text{sei}}[\Omega]$ . For this purpose, seismic acceleration  $S_a^{\text{sei}}$  is measured and low-pass filtered to obtain  $S_x^{\text{sei}}[\Omega] = S_a^{\text{sei}}[\Omega]/\Omega^4$ .

Figure 7 shows the coherence spectrum,  $|S_{\theta x}^{\text{sei}}[\Omega]|^2 / S_{\theta}[\Omega] S_x^{\text{sei}}[\Omega]$ , between angular displacement and seismic noise. A relatively high coherence is observed in the range of 300 Hz – 1 kHz, resembling the excess noise seen in Fig. 2(a) of the main text. Therefore, the noise peaks in this frequency range are likely attributable to seismic noise, while the long-term noise below 300 Hz may be caused by air current-induced refractive index fluctuations.

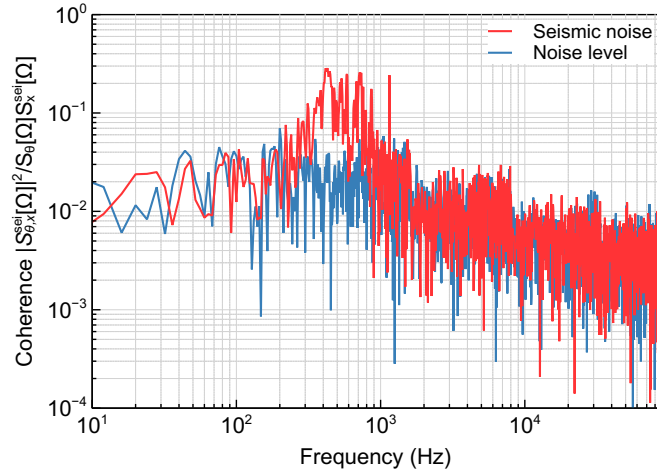


FIG. 7. Coherence spectrum between angular displacement and seismic noise.

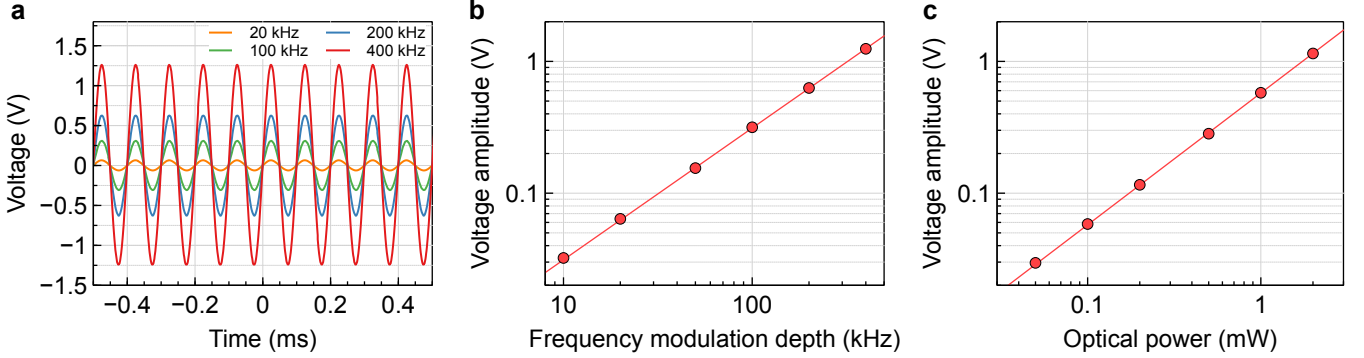


FIG. 8. Characterization of the acousto-optic deflector (AOD)-based voltage-to-angle calibration. (a) Sinusoidal frequency modulation of the AOD drive leads to a corresponding modulation in the signal detected by the single-photon detector (SPD) in the time domain. To minimize extraneous noise and improve the accuracy of the voltage amplitude estimation, the SPD signal is triggered and averaged over 100 iterations. (b) The relationship between the frequency modulation depth (corresponding to beam tilt amplitude) and the SPD signal is linear, with a coefficient of determination  $R^2 = 0.9996$ . The incident optical power on the SPD is  $500 \mu\text{W}$ . (c) A linear relationship also exists between the optical power and the SPD signal amplitude, with the AOD drive modulation depth set to 100 kHz.

## Appendix D: Angle calibration

### 1. Calibration of mirrored optical lever

In conventional optical lever techniques, the angular displacement of the torsion pendulum,  $\delta\theta$ , is inferred from the geometry of the lever: a laser beam deflected with a tilt of  $2\delta\theta$  propagates over a distance  $z$ , thereby amplifying the transverse displacement by the lever arm, i.e.,  $\delta x = 2z\delta\theta$ . This suggests that extending the lever arm could infinitely amplify the SPD signal gain. However, this naive calibration is only valid within the framework of ray optics; beyond the Rayleigh length of the laser beam, the gain of the SPD signal eventually saturates.

For accurate measurement of the intrinsic thermal motion of a high- $Q$  torsion pendulum, calibration is often performed by fitting the theoretical model of thermal motion to the SPD voltage spectrum. However, this method can lead to inaccuracies when extraneous noise, such as photothermal effects or external disturbances, contaminates the angular displacement spectrum.

To overcome this limitation, we employ a direct calibration method that relates the SPD signal to angular displacement using an acousto-optic deflector (AOD). As described in the main text, an AOD (M1377-aQ80L-1, ISOMET) is positioned at the input plane of the entrance lens of a  $4f$  imaging system, with the torsion pendulum (and retroreflector) located at the output plane of the second lens. The  $4f$  system, composed of two lenses with identical focal lengths,

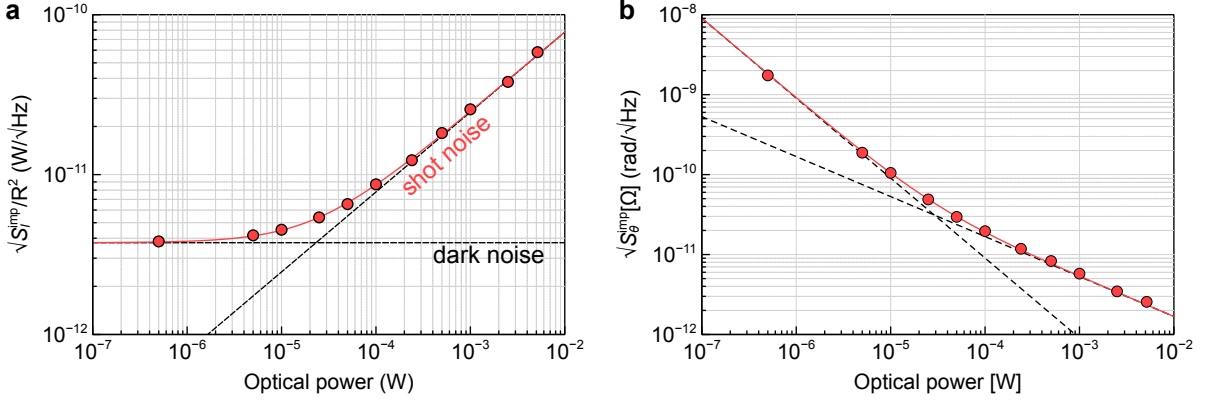


FIG. 9. (a) Input-referred photocurrent noise. (b) imprecision noise in angular displacement.

reproduces the angular tilt of the laser beam at the input plane at the output plane.

We use the first-order diffraction beam from the AOD, with its tilt angle precisely controlled by the relation  $\Delta\theta_{\text{cal}} = (\lambda/v_c)\Delta f_{\text{cal}}$ , where  $\Delta f_{\text{cal}}$  is the drive frequency change and  $v_c \approx 5700 \text{ m/s}$  is the acoustic velocity of the AOD quartz crystal. Using this relation, we determine the calibration factor for converting the SPD voltage spectrum into an angular displacement spectrum. Since the laser beam acquires an angular displacement that amounts to twice the torsional motion of the pendulum upon reflection, the calibration factor is defined as  $\alpha_{\text{cal}} = \Delta\theta_{\text{cal}}/2\Delta V_{\text{cal}}$ , where  $\Delta V_{\text{cal}}$  represents the voltage change in the SPD signal. To precisely attain the calibration factor, we frequency modulate the AOD drive with a known depth ( $\Delta f_{\text{cal}}$ ), and observe the corresponding SPD voltage modulation amplitude ( $\Delta V_{\text{cal}}$ ) in the time domain. In this process, we trigger and average the calibration tone 100 times to mitigate extraneous noises in the SPD signal. Then, the calibration factor is used to convert the SPD spectrum to the angular displacement spectrum:  $S_\theta[\Omega] = \alpha_{\text{cal}}^2 S_V[\Omega]$ , where  $S_V[\Omega]$  is the measured SPD spectrum. Our typical choice for the AOD calibration is a 10 kHz frequency modulation tone with a 100 kHz frequency depth (the corresponding tilt amplitude of 18.7  $\mu\text{rad}$ ), centered around 80 MHz (AOD operation frequency). Note that, although this calibration tone can be detected in the power spectral density (PSD), the measured voltage amplitude may be inaccurate or underestimated due to the broadening of the linewidth in the PSD analysis.

Fig. 8 illustrates the application of AOD-based calibration in our experiments. We vary the frequency modulation depth of the AOD drive and monitor the SPD signal in the time domain. The triggering and averaging of the modulation signal is performed by an oscilloscope (Moku:Pro, Liquid Instruments). The voltage amplitude is then estimated from these averaged data. Fig. 8(b) displays the voltage amplitudes as a function of modulation depths, corresponding to beam tilt amplitudes, which provides the calibration factor for converting the SPD spectrum into the angular displacement spectrum. The linear relationship is confirmed with a coefficient of determination  $R^2 = 0.99996$ . Additionally, Fig. 8(c) demonstrates the linear dependence of voltage amplitude on incident optical power.

Figure 2(b) in the main text is calibrated from the SPD voltage spectrum to the angular displacement spectrum using the calibration method described above. To verify that the imprecision noise in the spectrum is quantum-noise-limited, we measure the noise floor of the photocurrent density, referred back to the optical power, at a frequency of  $\Omega = 2\pi \cdot 80 \text{ kHz}$  under varying optical levels. As shown in Fig. 9(a), at power levels below 20  $\mu\text{W}$ , the dark noise is dominant, while shot noise starts to prevail beyond this threshold. The curve fitting reveals that the quantum efficiency of the balanced photodetector used in this study is 0.81. Fig. 9(b) shows the imprecision noise in the angular displacement obtained by implementing the calibration method. The beam width at the position of the flat mirror is 587  $\mu\text{m}$  measured by a beam profiler (BC207VIS, Thorlabs). The angular sensitivity improves as the optical power increases, and, at the maximum power of 5 mW, the imprecision noise reaches 2.56  $\text{prad}/\sqrt{\text{Hz}}$ . This value is 16% higher than the shot noise level (2.21  $\text{prad}/\sqrt{\text{Hz}}$ ) calculated under the assumption of ideal detection (Eq. (C4)). Therefore, the detection efficiency is 0.75.

## 2. Calibration of thermal noise spectra

When measuring the torsion pendulum, we reduced the beam size from 587  $\mu\text{m}$  to 180  $\mu\text{m}$  to minimize clipping loss of the measurement beam at the finite surface width of the pendulum (500  $\mu\text{m}$ ). This reduction was achieved by focusing the beam onto the AOD at the input plane of the 4f system. However, it was observed that the AOD

calibration method became inaccurate as the beam was focused onto the AOD crystal: despite applying a pure tone frequency modulation, the SPD signal was significantly distorted with harmonics. This appears to be due to the incoherent addition of diffraction angles as the beam is focused on the AOD crystal. To address this, we adopted a two-step calibration process: (1) calibrating the thermal motion of the torsion pendulum using a reliable, larger beam size ( $w_0 \approx 587 \mu\text{m}$ ), and (2) using this thermal motion as a reference to calibrate the SPD spectrum obtained with the smaller beam size ( $w_0 \approx 180 \mu\text{m}$ ). The second step was performed with 1 mW optical power, which kept the pendulum at room temperature (290 K) (see Appendix E 4). The calibration factor was determined by fitting the spectra to the thermal noise at room temperature, resulting in a calibration factor of  $\alpha_{\text{cal}} = 1.65 \times 10^{-9} \text{ rad/V}$  with a 2% error.

Through two-step calibration, the imprecision noise at the SPD was found to be  $S_{\theta}^{\text{imp}} = 1.06 \times 10^{-22}$  at 10 mW optical power, corresponding to a detection efficiency of 0.244. The lower sensitivity is largely due to the reduced beam size (Eq. (C3)).

The ideal imprecision derived in (Eq. (C3)), which assumes an intact spatial mode profile upon reflection, does not hold for the torsion pendulum measurement: that derivation assumes that tilt is induced by an infinite plane, whereas the finite extent of the torsion pendulum clips the wings of the Gaussian beam, leading to distortion of the reflected beam beyond the simple model. Nonetheless, the imprecision noise shown in Fig. 3(a) of the main text is quantum-noise-limited, as confirmed by its good agreement with the expected shot noise scaling (Eq. (C3)).

## Appendix E: Measurement-based feedback cooling

### 1. Theory

The physical angular displacement of the torsion pendulum reacts to external torques, consisting of thermal, back-action, and feedback torques:

$$\chi_0^{-1}[\Omega] \delta \hat{\theta}_{\text{phys}}[\Omega] = \delta \hat{\tau}_{\text{th}}[\Omega] + \delta \hat{\tau}_{\text{ba}}[\Omega] + \hat{\tau}_{\text{fb}}[\Omega], \quad (\text{E1})$$

where  $\chi_0[\Omega]$  is the susceptibility of the torsion pendulum. In measurement-based feedback control [25, 26], the observed motion [Eq. (B17)]

$$\delta \hat{\theta}_{\text{obs}}[\Omega] = \delta \hat{\theta}_{\text{phys}}[\Omega] + \delta \hat{\theta}_{\text{imp}}[\Omega] \quad (\text{E2})$$

is used to synthesize a feedback force, in this case a torque,

$$\delta \hat{\tau}_{\text{fb}}[\Omega] = -\chi_{\text{fb}}^{-1}[\Omega] \delta \hat{\theta}_{\text{obs}}[\Omega] \quad (\text{E3})$$

so that the physical motion

$$\delta \hat{\theta}_{\text{phys}}[\Omega] = \chi_{\text{eff}}[\Omega] (\delta \hat{\tau}_{\text{tot}}[\Omega] - \chi_{\text{fb}}^{-1}[\Omega] \delta \hat{\theta}_{\text{imp}}[\Omega]) \quad (\text{E4})$$

is modified via the effective susceptibility  $\chi_{\text{eff}} = (\chi_0^{-1} + \chi_{\text{fb}}^{-1})^{-1}$ ; here  $\delta \hat{\tau}_{\text{tot}} = \delta \hat{\tau}_{\text{th}} + \delta \hat{\tau}_{\text{ba}} + \delta \hat{\tau}_{\text{fb}}$ . In the presence of feedback, the observed motion is also modified:

$$\delta \hat{\theta}_{\text{obs}}[\Omega] = \chi_{\text{eff}}[\Omega] (\delta \hat{\tau}_{\text{tot}}[\Omega] + \chi_0^{-1}[\Omega] \delta \hat{\theta}_{\text{imp}}[\Omega]) \quad (\text{E5})$$

Cooling by this kind of feedback can be affected by the choice  $-\chi_{\text{fb}} = iI\Omega\Gamma_{\text{fb}}$  around mechanical resonance  $\Omega_0$ . In this case, the spectrum of the observed motion assumes the form

$$S_{\theta}^{\text{obs}}[\Omega] = \frac{S_{\tau}^{\text{tot}}[\Omega]}{I^2[(\Omega_0^2 - \Omega^2)^2 + (\Omega\Gamma_{\text{eff}})^2]} + \frac{(\Omega_0^2 - \Omega^2)^2 + (\Omega\Gamma_0[\Omega])^2}{(\Omega_0^2 - \Omega^2)^2 + (\Omega\Gamma_{\text{eff}})^2} S_{\theta}^{\text{imp}}[\Omega]; \quad (\text{E6})$$

this model is used to fit the data in Fig. 3 of the main text. The spectrum of the physical motion

$$S_{\theta}^{\text{phys}}[\Omega] = \frac{S_{\tau}^{\text{tot}}[\Omega]}{I^2[(\Omega_0^2 - \Omega^2)^2 + (\Omega\Gamma_{\text{eff}})^2]} + \frac{(\Omega\Gamma_{\text{fb}})^2}{(\Omega_0^2 - \Omega^2)^2 + (\Omega\Gamma_{\text{eff}})^2} S_{\theta}^{\text{imp}}[\Omega], \quad (\text{E7})$$

allows inference of physical properties such as the average phonon occupation achieved by feedback cooling.

If we take the torsional motion to be a harmonic oscillator with creation/annihilation operators  $\hat{b}, \hat{b}^\dagger$ , then the angular motion is  $\hat{\theta} = \theta_{\text{zp}}(\hat{b} + \hat{b}^\dagger)$ , where  $\theta_{\text{zp}} = \sqrt{\hbar/(2I\Omega_0)}$ . Then the variance of the motion is  $\langle \hat{\theta}^2 \rangle = 2\theta_{\text{zp}}^2 (\langle \hat{b}^\dagger \hat{b} \rangle + \frac{1}{2})$ ; thus the phonon occupation  $n_{\text{eff}} = \langle \hat{b}^\dagger \hat{b} \rangle$  can be inferred from the variance of the (physical) angular motion via

$$n_{\text{eff}} + \frac{1}{2} = \frac{\langle \hat{\theta}^2 \rangle}{2\theta_{\text{zp}}^2} = \int \frac{S_{\theta}^{\text{phys}}[\Omega] d\Omega}{2\theta_{\text{zp}}^2 2\pi}. \quad (\text{E8})$$

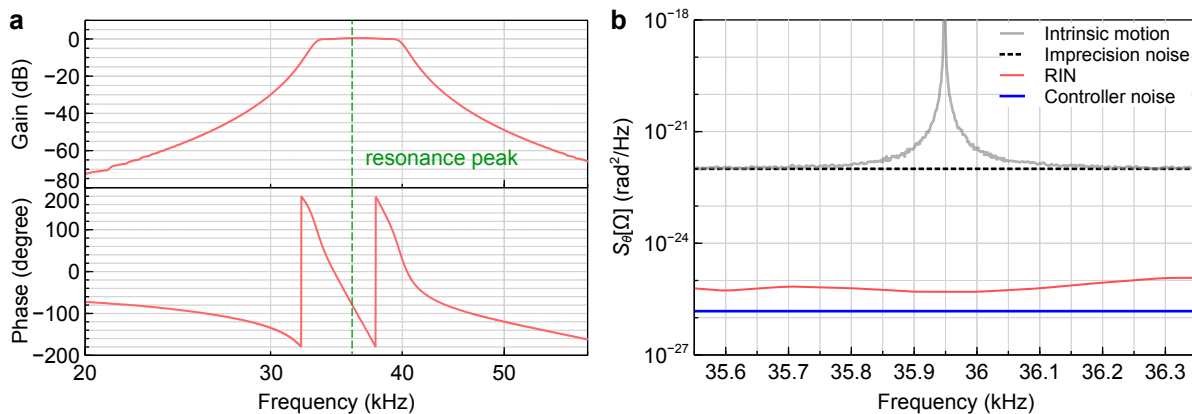


FIG. 10. (a) Frequency response of the feedback controller. (b) Angular displacement-referred extraneous noises in the feedback loop.

Using the model in Eq. (E7) gives

$$n_{\text{eff}} + \frac{1}{2} = \left( n_{\text{th}} + n_{\text{ba}} + \frac{1}{2} \right) \frac{\Gamma_0}{\Gamma_{\text{eff}}} + n_{\text{imp}} \frac{\Gamma_{\text{eff}}}{\Gamma_0}, \quad (\text{E9})$$

where  $n_{\text{ba}} = S_{\tau}^{\text{ba}}[\Omega_0]/(4\hbar \text{Im} \chi_0^{-1}[\Omega_0])$  is the effective back-action phonon occupation, and  $n_{\text{imp}} = S_{\theta}^{\text{imp}}/(2S_{\theta}^{\text{zp}}[\Omega_0])$  is the phonon-equivalent measurement imprecision.

## 2. Implementation of feedback

The motion of the pendulum is actuated by radiation torque from a secondary laser beam (“actuation beam”) focused on the edge of the pendulum’s backside. A fiber-coupled electro-optic Mach-Zehnder amplitude modulator (LNx1020A, Thorlabs) is employed to modulate the radiation torque around the mechanical frequency. The modulator’s response to the external voltage is sinusoidal due to the nature of the Mach-Zehnder interferometer in it; we bias the modulator around its linear operating point, which corresponds to the bias voltage at which half the maximum optical power is transmitted. At this operating point, the actuation beam exhibits a sensitivity of 15.7 mW/V in response to the external voltage applied on the modulator.

Figure 10(a) is the measured frequency response of the feedback filter  $\chi_{\text{fb}}^{-1}$ , optimized for feedback gain to achieve a phonon number of approximately 6000. This configuration is implemented using an FPGA-based controller (Moku:Pro, Liquid Instruments). The feedback filter comprises a bandpass filter (34–40 kHz) centered around the resonance frequency of the fundamental mode, and a phase delay that aligns the total loop delay to be  $\pi/2$ . As depicted in Fig. 10(a), the delay at the resonance frequency  $\Omega_0/2\pi = 35.95$  kHz is precisely set to  $\pi/2$ .

## 3. Extraneous noise in feedback

Extraneous noise in the feedback loop can limit the performance of feedback cooling if they are larger than the imprecision noise in the measurement that drives the actuator. We investigate this possibility by measuring and budgeting the noise in the actuator beam. Figure 10(b) shows this budget referred to angular displacement at the SPD. Two contributions can be distinguished: (a) voltage noise from the feedback controller, referred to angle (blue); and, (b) intensity noise in the actuation beam referred to angle (red). Grey shows the motional signal at the SPD, with black dashed showing the quantum-noise-limited imprecision. Clearly, the extraneous noise in the feedback loop lies more than 30 dB below the imprecision noise. Thus, feedback cooling is governed primarily by the observed motion.

Next, we investigate whether the actuation beam induces mechanical torques in excess of that due to radiation pressure. For example, thermoelastic torques [34, 35] arising from concentrated photothermal heating at the edge of the torsion pendulum. The nature of the thermoelastic effect can be understood through the absorption and diffusion of heat within the pendulum. This suggests that the thermoelastic effect can be distinguished from pure radiation pressure torque [36, 37]: the angular displacement response to thermoelastic torque follows a single-pole low-pass filter characteristic at a specific cutoff frequency, while the radiation pressure torque remains frequency-independent.

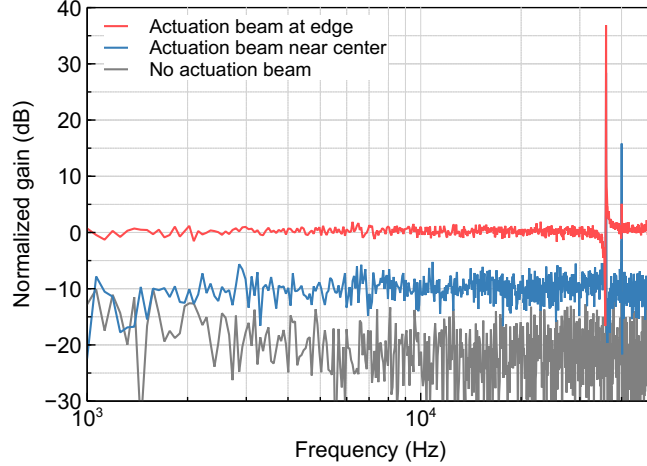


FIG. 11. Frequency response of angular displacement of the torsion pendulum to the radiation pressure torque actuator.

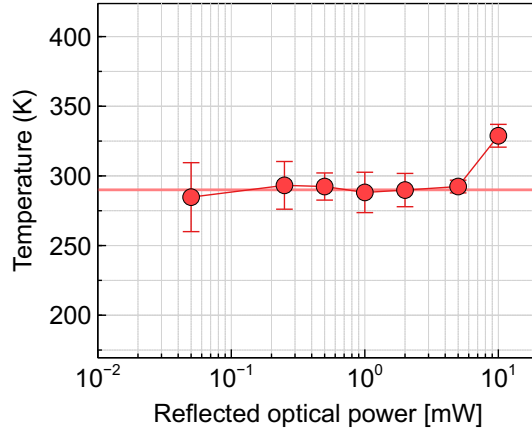


FIG. 12. Estimation of mode temperature using the AOD-based calibration method.

Figure 11 is the frequency-response of the torsion pendulum as the intensity in the actuator beam is modulated. The response remains frequency-independent from 1 kHz up to the resonance for various beam positions, both at the edge and near the center of the pendulum. This suggests that no thermoelastic effect is observed during feedback actuation, and that the actuation is dominated by radiation torque.

#### 4. Estimation of mode temperature

To investigate the role of photothermal heating, we measured the mode temperature as a function of optical power (from now on, the optical power is referred to as that reflected from the torsion pendulum). For this, we fit the torsion pendulum's intrinsic motion to a Lorentzian model:  $S_{\theta}^{\text{obs}}[\Omega] = S_{\theta}^{\text{imp}} + S_{\theta}^{\text{th}}[\Omega_0]/(1 + 4Q_0^2(\Omega - \Omega_0)^2/\Omega_0^2)$ . Since the resolution bandwidth of the spectrum (0.25 Hz) is larger than the linewidth of the torsional mode ( $\Gamma_0/2\pi = 2.6$  mHz), we excluded the vicinity of the peak from the fitting range. Using these fittings, we estimated the mode temperatures shown in Fig. 12. For optical powers below 5 mW, no signs of photothermal heating were observed. The fits allow us to infer the effective moment of inertia  $I = 5.54 \cdot 10^{-17}$  kg  $\cdot$  m<sup>2</sup> with the independently measured values of  $\Omega_0 = 2\pi \cdot 35.95$  kHz,  $Q = 1.365 \cdot 10^7$ , and  $T = 290$  K. This value is 30% smaller than that obtained by finite element simulation (COMSOL Multiphysics), ( $7.87 \cdot 10^{-17}$  kg  $\cdot$  m<sup>2</sup>) and larger by 12% compared to the analytical model [17]  $I = \rho Lhw^3/24 \approx 4.91 \cdot 10^{-17}$  kg  $\cdot$  m<sup>2</sup> of an ideal rectangular beam (which our device is not). This provides an independent consistency check of our angle calibration procedure and mode temperature.